Preparation of Mesoporous Sb-, F-, and In-Doped SnO_2 Bulk Powder with High Surface Area for Use as Catalyst Supports in Electrolytic Cells

*Hyung-Suk Oh, Hong Nhan Nong, and Peter Strasser**

The M-doped tin oxides (M = Sb, F, and In) to be used as catalyst support are synthesized by using templating process with tetradecylamine (TDA) as the template, combined with a hydrothermal (HT) method to improve its thermal stability. The obtained materials are characterized by XRD, SAXS, TEM, EDX, SEM, and BET to study microstructure and physical properties, which have a mesoporous structure, small particle size, and high surface area (125–263 $m^2\ g^{-1}$). The materials show an overall conductivity of 0.102–0.295 S cm^{-1}. Repetitive potential cycling is employed to characterize the electrochemical properties and stability. The M-doped tin oxides are highly electrochemical stable compared to carbon black. From the observed results, it can be concluded that the combination of TDA and HT treatment are an effective synthetic method for designing mesoporous M-doped tin oxide as catalyst supports.

1. Introduction

Precious metals (Pt, Ir, Pd, Au, Ru, and Ag) have been widely used for electrochemical catalysis in many industries.[1] In general, these catalysts are essential to use of support material to provide a physical surface for fine dispersion of metal nanoparticles, which is necessary for reducing the amount of precious metal.[2] Carbon black is the most frequently employed as support material because of its high surface area for the dispersion and stabilization of metal nanoparticles, bulk powder type for simple application in catalysts synthesis, a porous structure for facile mass transfer of reactants, and good electrical conductivity required for electrochemical reactions.[3] From a thermodynamic point of view, however, carbon is vulnerable to corrosive condition. The reported mechanism of carbon corrosion suggests that functional oxygen groups are generated on the carbon surface above 0.207 V (vs RHE), and in turn carbon converted to carbon dioxide (CO_2).[4] The carbon corrosion causes the release of precious metal particles, which become electrically isolated, leading to a significant decrease of the performance and operation lifetime of the catalysts.[5] To overcome this problem, many studies have concentrated on graphitized carbon such as carbon nanotube (CNT) and carbon nanofiber (CNF).[6] However, these materials still do not prevent irreversible carbon oxidation at high electrode potentials and heat-treatment for graphitization can increase processing costs.[7]

Therefore, various conductive metal oxides including WO_2, TiO_2, Nb_2O_5, SnO_2, and others have received much attention as candidates for oxidation resistant catalyst supports.[8] Among these candidates, doped tin oxide, such as tin doped indium oxide (ITO), antimony doped tin oxide (ATO), and fluorine doped tin oxide (FTO), have gained increasing attention as a catalyst supports due to their high electrical conductivity and electrochemical stability.[9] Bjerrum investigated the electrochemical stability of antimony doped tin oxide (ATO) nanoparticles as catalyst support for polymer electrolyte membrane (PEM) water electrolysis, and found that ATO had much higher corrosion resistance than carbon.[10] Mustain also suggested Pt adsorbed on ITO as an oxygen reduction reaction (ORR) catalysts. The prepared catalyst showed high catalytic activity and stability through synergistic effects between Sb surface and Pt.[9a] However, these metal oxides have low surface area (>48 $m^2\ g^{-1}$) compare with carbon black (Vulcan, 235 $m^2\ g^{-1}$), which prevent high loading and uniform dispersion of precious metal nanoparticles on the surface.

One approach to increase the surface area of doped metal oxide is Evaporation Induced Self-Assembly (EISA), which is useful in the formation of thin film type mesoporous structure.[11] However, it is difficult to load precious metal nanoparticles on thin film structure, even though its high surface area. Another widely used method is sol–gel method with organic surfactant.[12] The pioneer work on the synthesis of mesoporous metal oxide powder was done by Antonelli, where they used a tetradecyl-phosphate as surfactant.[13] In their report, TiO_2 calcined to 350 °C have narrow pore size and surface areas of 200 $m^2\ g^{-1}$. Following this approach, the synthesis of mesoporous SnO_2 by applying various surfactants and process modification was attempted at several groups.[14] However, the mesoporous structure was easily collapsed upon calcination at 400 °C due to the decomposition of surfactant before crystallization, and hence the surface area of metal oxide was decreased.[15] To improve the thermal stability, Chen used the neutral surfactant resulting in the stable mesoporous tin oxide up to 500 °C, but surface area (107 $m^2\ g^{-1}$) was much smaller than those of carbon black.[14b] Zhu also used the tetradecylamine (TDA) as

Dr. H.-S. Oh, H. N. Nong, Prof. P. Strasser
The Electrochemical Energy
Catalysis, and Materials Science Laboratory
Department of Chemistry
Chemical Engineering Division
Technical University Berlin
Berlin 10623, Germany
E-mail: pstrasser@tu-berlin.de

DOI: 10.1002/adfm.201401919

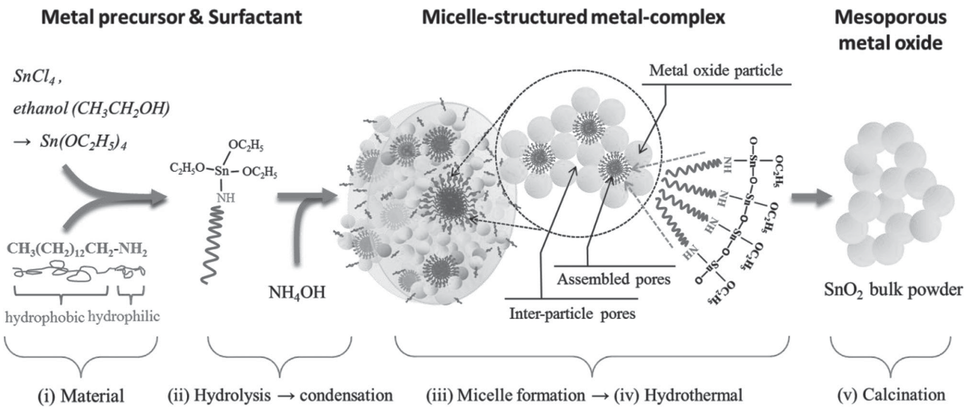

Figure 1. Synthesis pathway of mesoporous metal oxide bulk powder: i) Material, ii) Hydrolysis and condensation, iii) Micelle formation, iv) Hydrothermal, and v) Calcination.

template and the tetraethylothosilicate (TEOS) as crystal growth inhibitor.[14d] The synthesized SnO_2 had very large specific surface area (211–339 m^2 g^{-1}) at temperature from 400 to 600 °C, however these were barely unsuitable for the electrocatalyst supports because nonconductive silicon dioxide remained in the metal oxide structure. Furthermore, there are only a few reports about doped SnO_2 powder with high surface area and homogeneity, because the constituent metals of mixed metal oxide exhibit different hydrolysis and condensation kinetics.[16] From these considerations and for all practical purposes, a more viable synthetic approach is required.

Here, we describe a simple wet-chemical method that enables the synthesis of doped tin oxide (ATO, FTO, and ITO) bulk powder with high surface area, high crystalline, and mesoporous structure. We have shown that neutral surfactant can act as structure directing agents for mesoporous structure and thermal stability is enhanced by hydrothermal process. The physical and electrochemical properties of these metal oxides were characterized using various techniques. Based on these results, the roles of surfactant and electrochemical stability are analyzed that can serve to guide the preparation of better doped tin oxide as catalyst supports.

2. Results and Discussion

Mesoporous SnO_2 bulk powder with high surface area was synthesized using the combined method with sol–gel and hydrothermal treatment. The overall process is illustrated in **Figure 1** and involved the following step. (i) Formation of complex from metal precursor and tetradecylamine (TDA) as surfactant agent: $SnCl_4$ vigorously reacts with ethanol to form tin ethobutoxide, as indicated by the following reaction:

$$SnCl_4 + 4CH_3CH_2OH \rightarrow Sn(OC_2H_5)_4 + 4HCl$$

Tin ethobutoxide in acidic ethanol solution is slowly hydrolyzed and assembled with TDA surfactant. (ii) Hydrolysis and condensation step: during refluxing of the mixture, white precipitates started to be observed and ammonium hydroxide (NH_4OH) promoted hydrolysis and condensation. (iii) The micelles of the TDA template with metal oxide into a disordered mesophase: related mesoporous structures have been obtained through S^oI^o assembly, wherein S^o is an alkylamine (TDA) and I^o is a tin ethobutoxide. TDA further enhances the binding affinity of the metal oxide nanoparticles to the amine functional group by hydrogen energy bonding. The micelles were composed of a core of relatively hydrophobic alkyl part and a shell of hydrophilic amine-metal oxide complex. (iv) Hydrothermal treatment: HT treatment was performed to prepare the nanocrystalline structure before calcination step, which improved the thermal stability. As shown in Figure S1 (Supporting Information), the XRD pattern of HT treated SnO_2 is highly crystalline and matches well with the tetragonal rutile SnO_2 structure. (v) Calcination step: the TDA template is thermally decomposed in air to leave behind mesoporous SnO_2 structure. The resulting tin oxide was denoted as SnO_2 with TDA, with HT, and its particle size was few changes compared with those of HT treated SnO_2. To understand the role of TDA and HT treatment, the synthesized SnO_2 was compared with HT treatment and TDA individually unapplied SnO_2, which were designated SnO_2 with TDA, without HT and SnO_2 without TDA, with HT, respectively.

The crystal structures of three different SnO_2 were measured using X-ray diffraction (XRD) technic and the results shown in **Figure 2**. In all three patterns, the evolution of the main peaks around $2\theta = 26.6°$, 33.9° and 51.8° are ascribed to the (110), (101), and (211) planes of the tetragonal rutile SnO_2 structure (JCPDS 21–1250 file).[17] The particle size was calculated by Scherrer equation and SnO_2 with TDA, with HT shows the smallest particle size of 2.3 nm compared to SnO_2 with TDA, without HT (3.1 nm) and SnO_2 without TDA, with HT (6.8 nm).

Figure 3 shows the HR-TEM images (a–c) and the particle size-distribution (d–f) of three different SnO_2. The photographs of metal oxide bulk powders were inset in Figure 3d–f, respectively. When comparing the particle size of these materials, the smallest particle size of 2.6 nm was observed in SnO_2 with TDA, with HT (Figure 3a) compared with SnO_2 with TDA, without HT (Figure 3b, 3.9 nm) and SnO_2 without TDA, with HT (Figure 3c, 8.9 nm). The micromorphologies and particle sizes were also examined by SEM. As seen from the Figure S2 (Supporting Information) that samples are composed with very tiny spherical nanoparticles. The trend of particle size is in the same line of the respective TEM images. These results are in

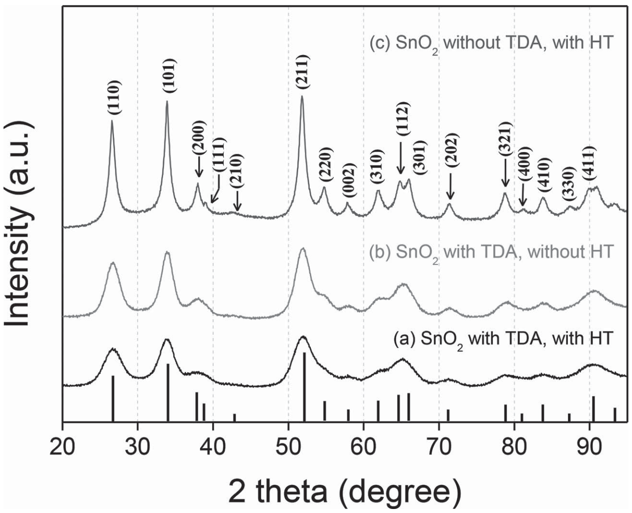

Figure 2. Wide-angle XRD patterns of mesoporous tin oxide bulk powder with different synthesis condition. a) SnO_2 with TDA, with HT, b) SnO_2 with TDA, without HT, and c) SnO_2 without TDA, with HT.

agreement with XRD data and easily rationalized by explanation with hydroxyl functional group and surfactant. In general, it is well known that hydroxyl functional groups of metal oxide were the main cause of crystal size growth during calcination process.[14b,18] Base on this knowledge, HT treatment practically diminished the excess oxygen functional groups on surface, which suppressed the increasing of particle size.[19] In case of TDA, it acts as a surfactant, which is a role to reduce the particle size of metal oxide.[14d]

The TEM images also provide insights into the structural features of mesopore. As shown in Figure 3a, although disordered, the porosity of SnO_2 with TDA, with HT homogeneously distributed over the entire structure and pore size was a range from 2 to 20 nm. This structure was consisted with the metal oxide nanoparticles, which were connected like a necklace and surrounded a space, resulted in the formation of disordered mseopores. In Figure S3 (Supporting Information), the mesoporous structure can be confirmed in more detail and the well-defined lattice planes prove the high crystallinity of the pore walls. On the contrary, TEM image of the SnO_2 with TDA, without HT (Figure 3b), shows a small pore size due to increasing of particle size in one direction along the pore walls preferentially. The sintering of nanoparticles within the pore walls leads to slight mesopore shrinkage and collapse. For SnO_2 without TDA, with HT (Figure 3c), tin oxide crystals are intimately connected and the pore is only constituted textural porosity due to the voids between the particles.

In order to expound the mesoporous structure of the synthesized SnO_2, nitrogen adsorption-desorption isotherms were analyzed, and the results are shown in **Figure 4**a and **Table 1**. All three samples show typical IV curves with hysteresis loops characterized by mesoporous materials.[20] Furthermore, a hysteresis loop at relative pressure (P/P_0) below 0.8 resembled type H2, but those at higher pressure were similar to type H3. The type H2 hysteresis loop, associated with materials with complex interconnected network of pores of different size and shape, is usually taken as the indication for the presence of pores with narrow mouths or channel-like pores of relatively uniform size.[21] The type H3 loop characterizes slit shaped pores formed from aggregates of plate-like particles.[21a] Pore size distribution of the synthesized SnO_2 was calculated using the non-local density functional theory (NLDFT) model. The desorption branch of H2 hysteresis loop is generally steeper than the adsorption branch.[22] This phenomenon is considered as the signature of the occurrence of a percolation process during the emptying of disordered porous material, and desorption scanning curves do not follow the original desorption branch of the hysteretic isotherm.[23] The NLDFT model revealed that, in

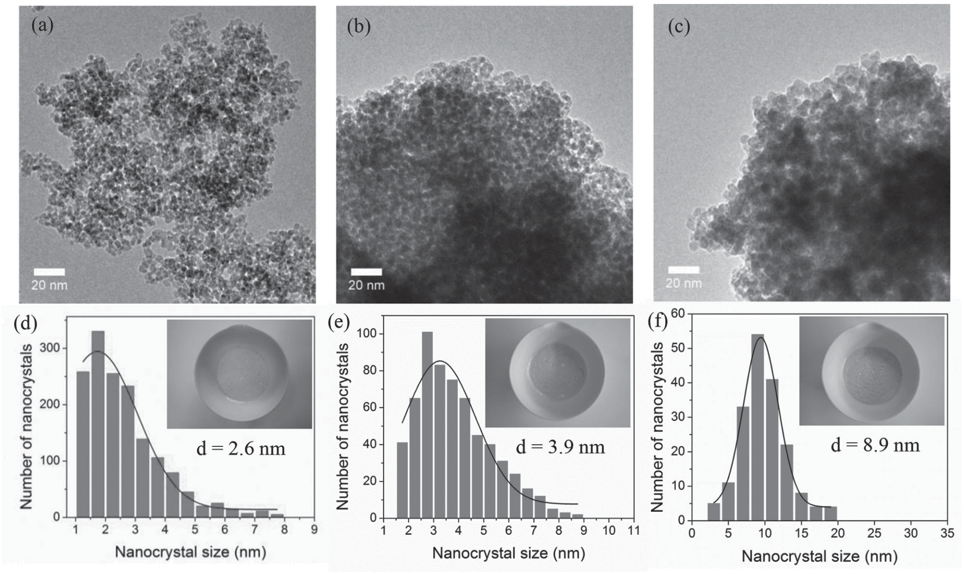

Figure 3. The physical property of mesoporous tin oxide bulk powder with different synthesis condition. TEM images of a) SnO_2 with TDA, with HT, b) SnO_2 with TDA, without HT, and c) SnO_2 without TDA, with HT, respectively. The corresponding size-distribution graphs (inset: the photographs of metal oxide bulk powder) of d) SnO_2 with TDA, with HT, e) SnO_2 with TDA, without HT, and f) SnO_2 without TDA, with HT, respectively.

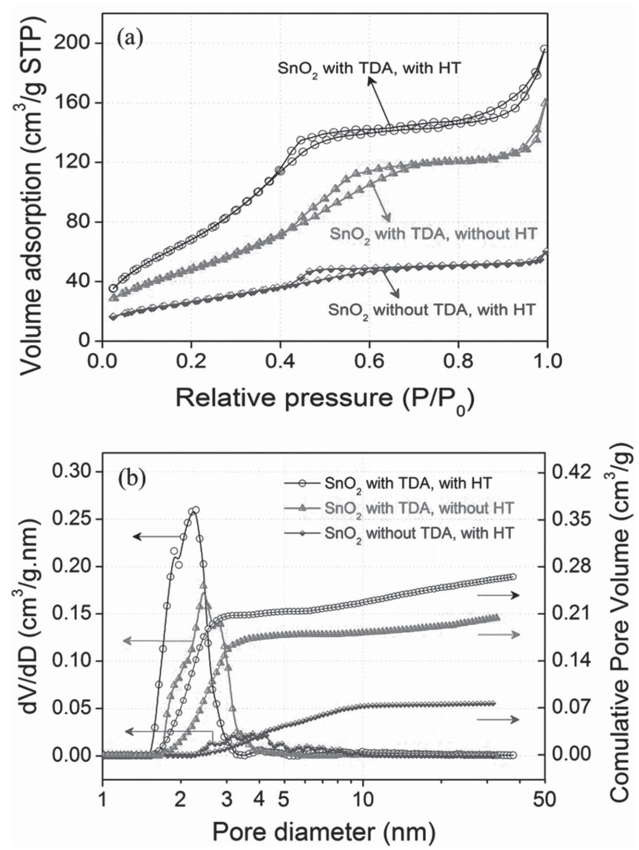

Figure 4. a) N_2 adsorption–desorption isotherm and b) NLDFT pore size distribution of mesoporous tin oxide bulk powder with different synthesis condition: i) SnO_2 with TDA, with HT, ii) SnO_2 with TDA, without HT, and iii) SnO_2 without TDA, with HT.

principle, both condensation and evaporation can be associated with metastable states of the pore fluid.[24] Hence, the NLDFT model was proper application to our synthesized metal oxides, and the applied results were shown in Figure 4b. SnO_2 with TDA, with HT exhibit rather pore diameter (2.8 nm) and high mesopore volumes (0.265 mL g^{-1}) as compared with SnO_2 with TDA, without HT (2.4 nm, 0.207 mL g^{-1}) and SnO_2 without TDA, with HT (1.8 nm, 0.078 mL g^{-1}). When comparing the surface area, SnO_2 with TDA, with HT showed the largest surface area of 290 m^2 g^{-1}. SnO_2 with TDA, without HT showed 187 m^2 g^{-1}, and the smallest surface area of 100 m^2 g^{-1} was observed in SnO_2 without TDA, with HT. These results summarized in Table 1.

The mesostructural features were also confirmed by small-angle XRD. As shown in **Figure 5**, SnO_2 with TDA, with HT has a single diffracted peak at low 2θ region and this is an evidence of the mesoporous structure.[25] The wall thickness of disordered mesopore was generally calculated by subtracting the pore diameter from *d*-spacing, and the results were summarized in Table 1.[26] The *d*-spacing and pore size of SnO_2 with TDA, with HT was 12.6 nm and 2.5 nm, respectively. The calculated wall thickness was 10.1 nm, which was almost 4.5-folder larger than mean particle size (2.3 nm). Therefore, we may conclude that the walls were comprised of aggregates with 4–5 SnO_2 nanoparticles, and the same trend was also shown in other groups.[14a,d] These were in good agreement with the results obtained from TEM (Figure S3, Supporting Information), which displayed an approximate pore-pore distance of ≈10 nm, a pore diameter of ≈2 nm, and wall thickness of ≈8 nm. As seen from the Figure S3 (Supporting Information) that the SnO_2 nanoparticles in the wall thickness part were agglomerated with 2–5 particles, which leads to the increase in the wall thickness and average *d*-spacing value in SAXS. For the removed hydrothermal step (SnO_2 with TDA, without HT), the single diffracted peak was also retained but shifted to lower 2θ angle. The calculated *d*-spacing and wall thickness were 17.3 nm and 14.9 nm, respectively, which were larger than those of SnO_2 with TDA, with HT. The incensement of both values is mainly caused by the crystal growth and coalescence, resulting in a destructed mesopore and formation of wormhole-like mesostructure.[14d] These were in agreement with HR-TEM and XRD results. On the other hand, the diffracted peak of SnO_2 without TDA, with HT in low 2θ region disappeared due to the relatively large grain growth which destroys the mesostructure. It can be concluded that the combined use of TDA as surfactant and HT treatment is an effective method of increasing both surface area and pore size by decreasing the particle size and wall thickness of metal oxide.

On the basis of these results, we proposed a generalized synthesis method for the doped tin oxide with high surface area, which was antimony doped tin oxide (ATO), fluorine doped tin oxide (FTO), and tin doped indium oxide (ITO), respectively. To prove the incorporation of the dopants into the SnO_2, EDX element mapping and element linescan performed in SEM. The

Table 1. Physical property of synthesized SnO_2 with different condition: (i) SnO_2 with tetradecylamine (TDA) and hydrothermal method (HT), (ii) SnO_2 with TDA and without HT, and (iii) SnO_2 without TDA and with HT.

Sample	Particle size in XRD [nm]	BET surface area [m^2 g^{-1}]	Average pore size[a)] [nm]	Pore volume[a)] [mL g^{-1}]	*d*-spacing in SAXS [nm]	Pore wall thickness[b)] [nm]
(i) SnO_2 with TDA, with HT	2.3	290	2.5	0.265	12.6	10.1
(ii) SnO_2 with TDA, without HT	3.1	187	2.4	0.207	17.3	14.9
(iii) SnO_2 without TDA, with HT	6.8	100	1.8	0.078	–	–

[a)] The nonlocal density function theory (NLDFT) model was used to calculate the average pore size and pole volume; [b)] Pore wall thickness calculated by subtraction of the NLDFT pore diameter from *d*-spacing.

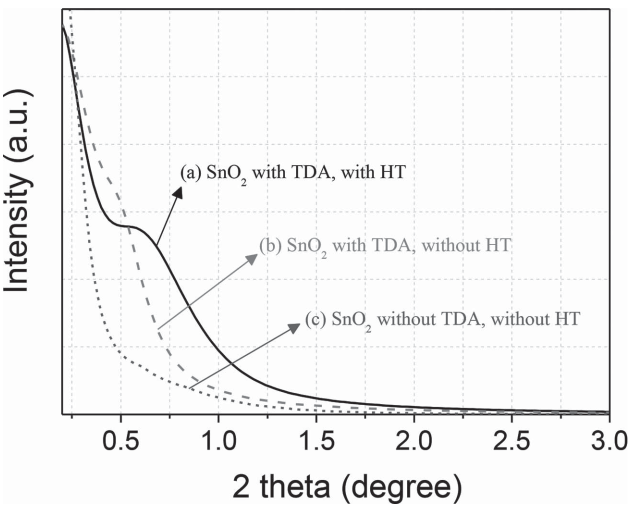

Figure 5. Small-angle XRD patterns of a) SnO$_2$ with TDA, with HT, b) SnO$_2$ with TDA, without HT, and c) SnO$_2$ without TDA, with HT, respectively.

Figure S4–S6 (Supporting Information) illustrate the nanoscale EDX elemental mapping of doped metal oxides and the appearance of the images confirmed the presence of Sn, Sb, F, and In elements are intimately interdispersed in the nanoscale. The element linescans also shows that dopants are uniformly distributed within the SnO$_2$ particles. Quantification of dopants from EDX was antimony (Sb) of 6.2 at% in ATO, fluorine (F) of 2.3 at% in FTO, and tin (Sn) of 9.1 in ITO, respectively. These results confirm that our method has been successful for synthesizing mesoporous doped metal oxides. XRD patterns also indicated that there was no phase separation within the crystals and all elements uniformly distributed into structure. As shown in Figure S7 (Supporting Information), the intensive diffraction peaks of ATO and FTO can be readily indexed to the tetragonal cassiterite structure of SnO$_2$ (JCPDS card no. 21–1250) and no diffraction peaks for Sb and F were observed. For ITO, the strong peak at 30.57° is the (222) peak for In$_2$O$_3$ (JCPDS card no. 6–0416) and no peak of SnO$_2$ was found in the XRD spectra. This means that doped ions were incorporated into the lattice of metal oxide.

TEM was used to verify the mesoporous structure and particle size of synthesized metal oxides, and the results were shown in **Figure 6**. As can be observed, these materials feature a mesoporous, foam like structure consisting of interconnected nanoparticles with monodispersity. However, the micropores were also indicated due to increasing particle size compared with SnO$_2$ by using TDA and HT treatment. When comparing the mean particle sizes, ATO showed the smallest particle size of 2.8 nm. FTO showed 3.2 nm, and the largest particle size of 8.1 nm was observed in ITO. These results are in good agreement with particle size in wide-angle XRD measurements (Figure S7, Supporting Information). Similar to the TEM images, the XRD measurements of the metal oxide powders also prove that they are crystalline.

The mesopore properties of the three different doped tin oxides were analyzed by gas physisorption in order to obtain information on both pore volume and specific surface area. **Figure 7**a shows the type IV isotherm with a type H3 hysteresis loop, which does not exhibit any limiting adsorption. This experiment gave evidence for the aggregates of porous structure with different sizes and shapes, is taken as the confirmation for the presence of partly micropores and slit shaped pores.[21] The precursors of tin doped metal oxides possess a different hydrolysis and condensation behavior, which leads to partial deformation of the mesoporous structure, creating a disordered nanostructure.[21a] This result is also confirmed with the observation from the TEM studies (Figure 6). The results of physisorption were summarized in Table S1 (Supporting Information), and the calculated BET surface area of ATO, FTO, and ITO

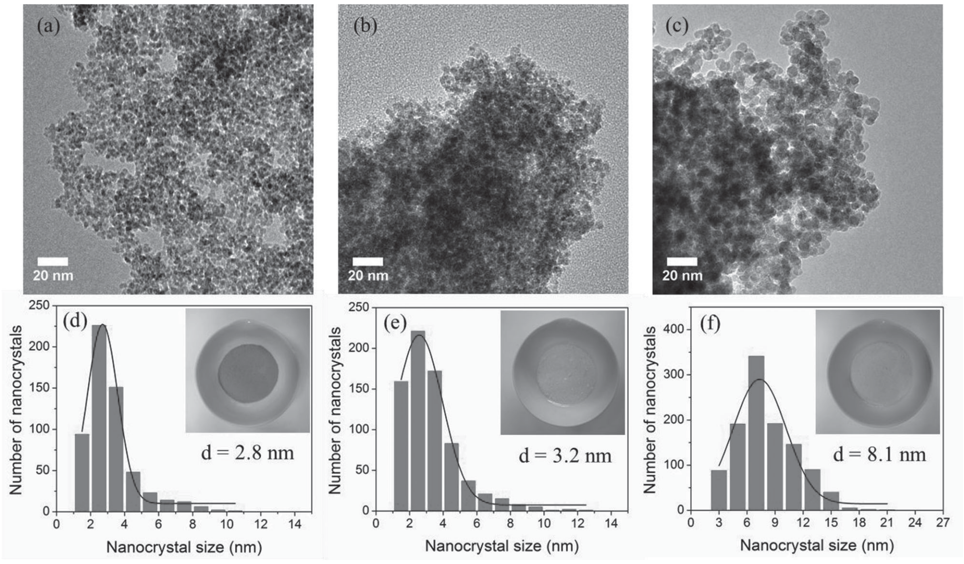

Figure 6. The physical property of mesoporous M-doped (M = Sb, F and In) tin oxide bulk powder. TEM images of a) antimony doped tin oxide (ATO), b) fluorine doped tin oxide (FTO), and c) tin doped indium oxide (ITO), respectively. The corresponding size-distribution graphs (inset: the photographs of metal oxide bulk powder) of d) ATO, e) FTO, and f) ITO, respectively.

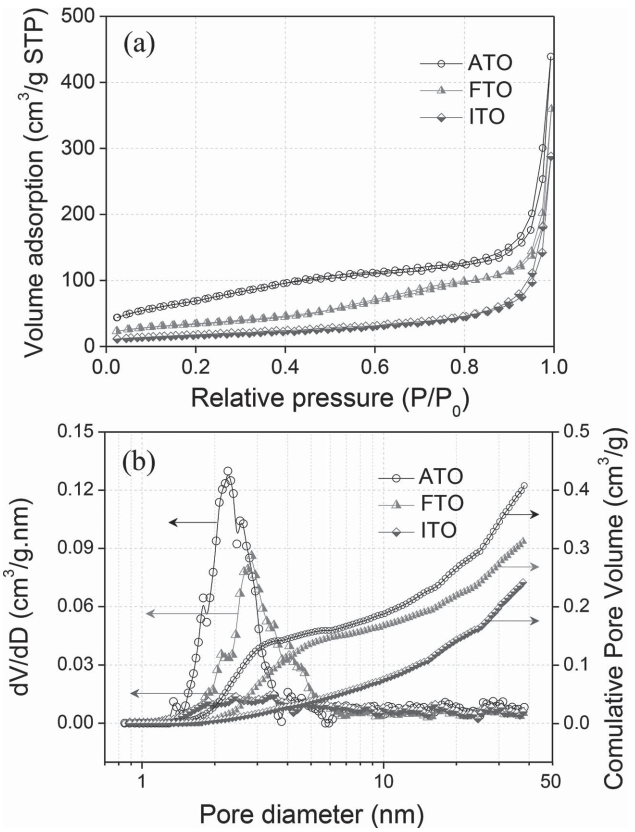

Figure 7. a) N_2 adsorption-desorption isotherm and b) pore size distribution of mesoporous tin doped metal oxide bulk powder: ATO, FTO, and ITO.

were 263, 173, and 125 m^2 g^{-1}, respectively. As shown Figure 7b, the pore sizes of tin doped metal oxides were slightly decreased compared with mesoporous SnO_2, because those particle sizes were increased. When comparing with Vulcan (235 m^2 g^{-1}, 0.554 mL g^{-1}), however, the surface area and pore volume are in a reasonable range for many applications as catalyst supports.

To verify the mesostructure of tin doped metal oxides, small-angle XRD measurements were conducted and the results shown in **Figure 8**. After the addition of dopants in SnO_2 structure, the mesostructure peaks were retained but the degrees were shifted to lower angle as compare to SnO_2 with TDA, with HT, which indicated the enlargement of *d*-spacing and wall thickness (Table S1, Supporting Information). In practice, the calculated *d*-spacing values of ATO (12.8 nm), ITO (15.7 nm), and FTO (27.6 nm) were larger than that of SnO_2 with TDA, with HT (12.6 nm). The calculated wall thickness of ATO, ITO, and FTO were 10.7 nm, 12.8 nm, and 24.1 nm, respectively, which were also thicker than that of SnO_2 with TDA, with HT (10.1 nm). This is presumably because the precursor of mixed metal oxides has a different hydrolysis and condensation rates, resulting in the formation of wormhole-like disordered mesopore by the crystal growth and coalescence.[27] These results were also in reasonable agreement with the HR-TEM (see Figure 6) and XRD (Figure S7, Supporting Information).

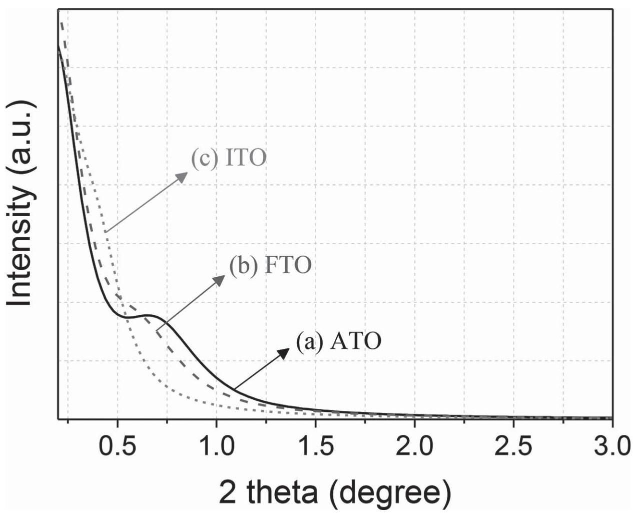

Figure 8. Small-angle XRD patterns of a) ATO, b) FTO, and c) ITO, respectively.

To evaluate the potential applicability in catalyst support, we investigated fundamental electrical conductivity and electrochemical stability of the as-synthesized tin doped metal oxides. The electrical conductivities of tin doped metal oxides were measured using four-point probe method and the results shown in Table S2 (Supporting Information). For comparison, undoped tin oxide (SnO_2) and carbon black (Vulcan) were also measured under same condition. The electrical conductivities of undoped tin oxide (SnO_2), antimony doped tin oxide (ATO), fluorine doped tin oxide (FTO), and tin doped indium oxide (ITO) were 0.0017, 0.295, 0.102, and 0.223 S cm^{-1}, respectively. It means that dopants were activated in the tin-doped metal oxides increases electrical conductivity. Although these values are lower than that of carbon black (Vulcan, 21.6 S cm^{-1}), it is sufficiently applicable to electrocatalyst supports because the minimum required electrical conductivity for selection of catalyst supports is 0.1 S cm^{-1}.[10,28]

The stability test was assessed using repetitive potential cycling experiments and the degradation of supports was evaluated by measuring the change of capacitance. In general, the capacitance of nonactive metallic oxides corresponds with the non-Faradaic double layer capacitance, which is related to the electrochemical surface area.[29] In this regard, the normalized capacitances of tin doped metal oxides were used as a measure of support surface area and monitored as a function of cycle number. For comparison, Vulcan was also tested under the same condition and the result was shown in **Figure 9**a. The capacitance of Vulcan initially increased to 2000 cycles, which showed evidence of considerable surface oxide formation through increased peak current assigned to the hydroquinone–quinone (HQ–Q) redox couple as shown in Figure S8a (Supporting Information).[3c,6a] After 2000 cycles of stability test, the capacitance consistently decreased because of the surface oxides were oxidized further to CO_2. In case of the tin doped metal oxides, however, the capacitances few changed upon cycling up 10 000 cycles. This result indicates that the metal oxide support is highly electrochemical stable. In Figure 9b is given the change of the total voltammetric charge (q_T^*) and electrochemical porosity before and after stability test, which were correlated with the electro active surface area and pore

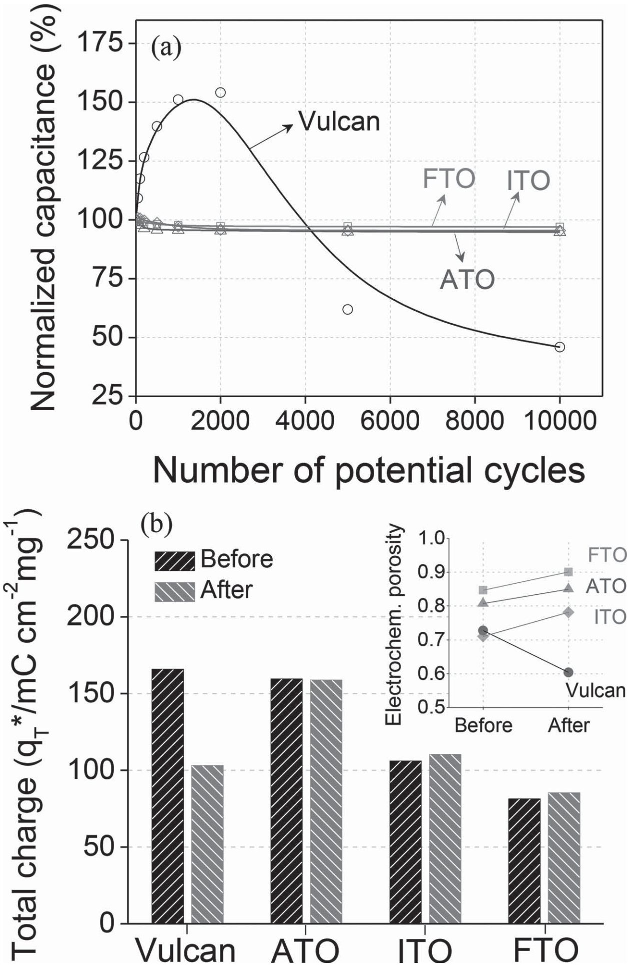

Figure 9. Electrochemical property of mesoporous tin doped metal oxides. For comparison, Vulcan was also analyzed under the same conditions. a) Change of normalized capacitance of the metal oxide as a function of cycle number. b) Change of the voltammetric charge corresponding to the total surface of tin doped metal oxide before and after stability test. (Inset: change of the electrochemical porosity of tin doped metal oxide before and after stability test.)

structure of supports.[30] These values were calculated based on the Figure S9 and S10, and the detail calculation method was indicated in Supporting Information. For Vulcan, total voltammetric charge and electrochemical porosity were decreased after stability test. On the contrary, those of metal oxides were remained or slightly increased. These results are in good accord with those capacitance changes, which were summarized in Table S3 (Supporting Information). It is obvious that the synthesized tin doped metal oxides would be more stable than Vulcan, which is appropriate to apply as catalyst supports.

3. Conclusion

In conclusion, we successfully synthesized mesoporous tin oxide bulk powder with high surface area (290 m^2 g^{-1}) and crystallized framework by a combined method with sol–gel and hydrothermal treatment (HT). Tetradecylamine (TDA) acts as a template agent and HT treatment reduced the oxygen groups on surface, which is a role to reduce the particle size and inhibit the collapse of pore structure. This process was also applied in the production of M-doped tin oxides (M = Sb, In, F), which were analyzed the physical and electrochemical property to evaluate the potential as catalyst supports. The obtained tin doped metal oxides show a high surface area (125–263 m^2 g^{-1}) and pore volume (0.242–0.408 mL g^{-1}). M-doped tin oxides exhibited an overall conductivity of 0.102–0.295 S cm^{-1} by four-point probe method. The electrochemical stability was evaluated by potential cycling at a sweep rate of 500 mV s^{-1} for up to 10 000 cycles. The doped tin oxides were highly electrochemical stable compared to carbon black. Therefore, it can be believed that combined method with surfactant and HT treatment can be used as a general synthetic method for designing mesoporous doped metal oxide as catalyst supports.

4. Experimental Section

Preparation of Mesoporous Metal Oxides: Mesoporous tin oxide (SnO$_2$) was prepared by following procedure. Tetradecylamine (TDA, 95.0%, 1.28g, Sigma–Aldrich) was added to an ethanol solution (EtOH 65 mL, D.I. water 160 mL) and the stirring was continued for 3 h. Tin tetrachloride (SnCl$_4$, 99.995%, 5.21g, Sigma–Aldrich) dissolved in ethanol (20 mL) was slowly added to the above suspension, and the mixture was stirred for 1 h. The mixture solution consisting of metal precursor and surfactant was added dropwise to 200 mL ammonium hydroxide solution (1.5 mmol L^{-1}) followed by stirring for 1 h. Subsequently, the resulting suspension was refluxed for 72 h at 80 °C and then cooled down to room temperature. The white precipitate was separated with solution by centrifugation at 5000 rpm for 10 min and then washing was repeated 5 times. The as-prepared wet samples were transferred to a glass-lined stainless-steel autoclave and hydrothermally treated at 120 °C for 24 h. In order to remove excess surfactant, final product was filtered and washed with ethanol for 5 times by using centrifuge after hydrothermal (HT) treatment. Produced white powder was dried in a freeze dryer and then drying sample was calcined at 400 °C for 3 h in air condition. The resulting metal oxide was designated as SnO$_2$ with TDA, with HT. For comparisons, SnO$_2$ with TDA, without HT and SnO$_2$ without TDA, with HT were also synthesized. The preparation of SnO$_2$ with TDA, without HT was the same as described above except for not applying hydrothermal method. For the SnO$_2$ without TDA, with HT, the same procedure was again followed without using tetradecylamine (TDA). Mesoporous antimony doped tin oxide (ATO), fluorine doped tin oxide (FTO) and tin doped indium oxide (ITO) were also synthesized follow the above procedure, which was only different the composition and kind of metal precursors. Detail methods were described in the Supporting Information.

Physical Characterization: Transmission electron microscopy (TEM, FEI Tecnai G2 20 S-TWIN, 200 kV) images were performed to observe structure and particle size of synthesized metal oxides. The surface morphology of the metal oxide was analyzed by scanning electron microscope (SEM, JEOL 7401F) at an acceleration voltage of 10 kV. SEM-EDX element mapping and element linescan were employed to study the element distribution and composition of metal oxide. Wide-angle X-ray diffraction (WAXD, Bruker D8 Advance instrument, Cu Kα radiation) and small-angle X-ray scattering (SAXS) were used to examine the crystal structure and identify the nature of metal oxides. The surface area was determined by nitrogen adsorption and desorption measurements (Quantachrome Autosorb-1-C). Brunauer Emmett Teller model (BET) formulations were used to calculate the surface area and nonlocal density functional theory (NLDFT) model was employed to analyze the pore size distribution of metal oxides. The electrical conductivity was measured using four-point probe method.

Electrochemical Analysis and Durability Test: Electrochemical characterization of metal oxides was performed using a rotating disk electrode (RDE, Pine Research instrument). The experiment was performed in a three-compartment electrochemical cell in 0.05 M H_2SO_4. A glassy carbon electrode with a thin film of the prepared sample was used as the working electrode. A platinum wire and mercury/mercurous sulfate (MMS, Hg/Hg_2SO_4) electrode were used as the counter and reference electrodes, respectively. The electrochemical stability and porosity of synthesized metal oxides were analyzed, and details about electrochemical protocols are provided in the Supporting Information.

Supporting Information

Supporting Information is available from the Wiley Online Library or from the author.

Acknowledgements

Financial support by the German Research Foundation (DFG) through Grant No. STR 596/3–1 under the Priority Program 1613 “Regeneratively formed fuels by water splitting” is gratefully acknowledged. The authors thank HZB for allocation of synchrotron radiation beamtime. The authors also thank Tobias Reier for help with the SEM measurement. The authors acknowledge the help of Dr. Ralph Krähnert and Benjamin Paul for help with the electrical conductivity measurement.

Received: June 11, 2014
Revised: November 26, 2014

---

[1] a) H. Renner, G. Schlamp, I. Kleinwächter, E. Drost, H. M. Lüschow, P. Tews, P. Panster, M. Diehl, J. Lang, T. Kreuzer, A. Knödler, K. A. Starz, K. Dermann, J. Rothaut, R. Drieselmann, C. Peter, R. Schiele, in *Ullmann's Encyclopedia of Industrial Chemistry*, Wiley-VCH Verlag GmbH & Co. KGaA, Germany **2000**; b) J. M. Toledo, J. Corella, A. Sanz, *Environ. Prog.* **2001**, *20*, 167; c) M. S. Saha, V. Neburchilov, D. Ghosh, J. Zhang, *Wiley Interdiscip. Rev.: Energy Environ.* **2013**, *2*, 31; d) I. Katsounaros, S. Cherevko, A. R. Zeradjanin, K. J. J. Mayrhofer, *Angew. Chem., Int. Ed.* **2014**, *53*, 102; e) S. Akbayrak, S. Özkar, *ACS Appl. Mater. Interfaces* **2012**, *4*, 6302.

[2] a) K.-i. Muto, N. Katada, M. Niwa, *Appl. Catal., A* **1996**, *134*, 203; b) G. Wang, G. Sun, Z. Zhou, J. Liu, Q. Wang, S. Wang, J. Guo, S. Yang, Q. Xin, B. Yi, *Electrochem. Solid-State Lett.* **2005**, *8*, A12; c) J. M. Planeix, N. Coustel, B. Coq, V. Brotons, P. S. Kumbhar, R. Dutartre, P. Geneste, P. Bernier, P. M. Ajayan, *J. Am. Chem. Soc.* **1994**, *116*, 7935; d) E. Auer, A. Freund, J. Pietsch, T. Tacke, *Appl. Catal. A* **1998**, *173*, 259.

[3] a) X. Bourrat, *Carbon* **1993**, *31*, 287; b) D. Pantea, H. Darmstadt, S. Kaliaguine, C. Roy, *Appl. Surf. Sci.* **2003**, *217*, 181; c) K. H. Kangasniemi, D. A. Condit, T. D. Jarvi, *J. Electrochem. Soc.* **2004**, *151*, E125.

[4] a) L. M. Roen, C. H. Paik, T. D. Jarvi, *Electrochem. Solid-State Lett.* **2004**, *7*, A19; b) J. Wang, G. Yin, Y. Shao, S. Zhang, Z. Wang, Y. Gao, *J. Power Sources* **2007**, *171*, 331; c) S. D. Knights, K. M. Colbow, J. St-Pierre, D. P. Wilkinson, *J. Power Sources* **2004**, *127*, 127; d) C. A. Reiser, L. Bregoli, T. W. Patterson, J. S. Yi, J. D. Yang, M. L. Perry, T. D. Jarvi, *Electrochem. Solid-State Lett.* **2005**, *8*, A273.

[5] a) L. Kim, C. G. Chung, Y. W. Sung, J. S. Chung, *J. Power Sources* **2008**, *183*, 524; b) K. Yasuda, A. Taniguchi, T. Akita, T. Ioroi, Z. Siroma, *J. Electrochem. Soc.* **2006**, *153*, A1599.

[6] a) Y. Shao, G. Yin, J. Zhang, Y. Gao, *Electrochim. Acta* **2006**, *51*, 5853; b) H.-S. Oh, H. Kim, *Adv. Funct. Mater.* **2011**, *21*, 3954.

[7] a) X. Wang, W. Li, Z. Chen, M. Waje, Y. Yan, *J. Power Sources* **2006**, *158*, 154; b) Y.-J. Ko, H.-S. Oh, H. Kim, *J. Power Sources* **2010**, *195*, 2623.

[8] a) E. Antolini, E. R. Gonzalez, *Solid State Ionics* **2009**, *180*, 746; b) R. Ganesan, J. S. Lee, *Angew. Chem. Int. Ed.* **2005**, *44*, 6557; c) X. Cui, J. Shi, H. Chen, L. Zhang, L. Guo, J. Gao, J. Li, *J. Phys. Chem. B* **2008**, *112*, 12024; d) T. Ioroi, Z. Siroma, N. Fujiwara, S.-i. Yamazaki, K. Yasuda, *Electrochem. Commun.* **2005**, *7*, 183; e) K.-W. Park, K.-S. Seol, *Electrochem. Commun.* **2007**, *9*, 2256; f) R. Ganesan, J. S. Lee, *J. Power Sources* **2006**, *157*, 217; g) E. Slavcheva, V. Nikolova, T. Petkova, E. Lefterova, I. Dragieva, T. Vitanov, E. Budevski, *Electrochim. Acta* **2005**, *50*, 5444.

[9] a) Y. Liu, W. E. Mustain, *J. Am. Chem. Soc.* **2012**, *135*, 530; b) H. Chhina, S. Campbell, O. Kesler, *J. Power Sources* **2006**, *161*, 893; c) C.-H. Han, S.-D. Han, J. Gwak, S. P. Khatkar, *Mater. Lett.* **2007**, *61*, 1701.

[10] J. Xu, Q. Li, M. K. Hansen, E. Christensen, A. L. Tomás García, G. Liu, X. Wang, N. J. Bjerrum, *Int. J. Hydrogen Energy* **2012**, *37*, 18629.

[11] a) A. Llordes, A. T. Hammack, R. Buonsanti, R. Tangirala, S. Aloni, B. A. Helms, D. J. Milliron, *J. Mater. Chem.* **2011**, *21*, 11631; b) T. Brezesinski, A. Fischer, K. i. Iimura, C. Sanchez, D. Grosso, M. Antonietti, B. M. Smarsly, *Adv. Funct. Mater.* **2006**, *16*, 1433.

[12] a) D. Gu, F. Schuth, *Chem. Soc. Rev.* **2014**, *43*, 313; b) F. Schüth, *Chem. Mater.* **2001**, *13*, 3184.

[13] D. M. Antonelli, J. Y. Ying, *Angew. Chem. Int. Ed. Engl.* **1995**, *34*, 2014.

[14] a) K. G. Severin, T. M. Abdel-Fattah, *Chem. Commun.* **1998**, 1471; b) F. Chen, M. Liu, *Chem. Commun.* **1999**, 1829; c) S. Zhou, S. Lu, Y. Ke, J. Li, *Mater. Lett.* **2003**, *57*, 2679; d) J. Zhu, B. Y. Tay, J. Ma, *Mater. Lett.* **2006**, *60*, 1003.

[15] a) Y.-Y. Lyu, S. H. Yi, J. K. Shon, S. Chang, L. S. Pu, S.-Y. Lee, J. E. Yie, K. Char, G. D. Stucky, J. M. Kim, *J. Am. Chem. Soc.* **2004**, *126*, 2310; b) M. Kang, D. Kim, S. H. Yi, J. U. Han, J. E. Yie, J. M. Kim, *Catal. Today* **2004**, *93–95*, 695.

[16] J. R. Szczech, M. A. Lukowski, S. Jin, *J. Mater. Chem.* **2010**, *20*, 8389.

[17] S. H. Sun, G. W. Meng, G. X. Zhang, T. Gao, B. Y. Geng, L. D. Zhang, J. Zuo, *Chem. Phys. Lett.* **2003**, *376*, 103.

[18] N.-L. Wu, C.-Y. Tung, *J. Am. Ceram. Soc.* **2004**, *87*, 1741.

[19] J. Zhu, B. Y. Tay, J. Ma, *J. Mater. Process. Technol.* **2007**, *192–193*, 561.

[20] a) S. J. Gregg, K. S. W. Sing, H. W. Salzberg, *J. Electrochem. Soc.* **1967**, *114*, 279C; b) S. Brunauer, L. S. Deming, W. E. Deming, E. Teller, *J. Am. Chem. Soc.* **1940**, *62*, 1723.

[21] a) S.-S. Chang, B. Clair, J. Ruelle, J. Beauchêne, F. Di Renzo, F. Quignard, G.-J. Zhao, H. Yamamoto, J. Gril, *J. Exp. Bot.* **2009**; b) N. A. Seaton, *Chem. Eng. Sci.* **1991**, *46*, 1895.

[22] M. Thommes, *Chem. Ing. Tech.* **2010**, *82*, 1059.

[23] a) G. Mason, *Proc. R. Soc. London. A: Math. Phys. Sci.* **1983**, *390*, 47; b) G. Mason, *Proc. R. Soc. London. A: Math. Phys. Sci.* **1988**, *415*, 453; c) T. Horikawa, D. D. Do, D. Nicholson, *Adv. Colloid Interface Sci.* **2011**, *169*, 40.

[24] a) A. V. Neimark, P. I. Ravikovitch, A. Vishnyakov, *J. Phys.-Condens. Matter* **2003**, *15*, 347; b) A. V. Neimark, P. I. Ravikovitch, *Microporous Mesoporous Mater.* **2001**, *44–45*, 697.

[25] S. K. Das, M. K. Bhunia, A. Bhaumik, *Dalton Trans.* **2010**, *39*, 4382.

[26] E. Prouzet, T. J. Pinnavaia, *Angew. Chem. Int. Ed.* **1997**, *36*, 516.

[27] K. Sinkó, *Materials* **2010**, *3*, 704.

[28] K.-S. Lee, I.-S. Park, Y.-H. Cho, D.-S. Jung, N. Jung, H.-Y. Park, Y.-E. Sung, *J. Catal.* **2008**, *258*, 143.

[29] R. Berenguer, C. Quijada, E. Morallón, *Electrochim. Acta* **2009**, *54*, 5230.

[30] a) F. Montilla, E. Morallón, A. De Battisti, J. L. Vázquez, *J. Phys. Chem. B* **2004**, *108*, 5036; b) C. P. De Pauli, S. Trasatti, *J. Electroanal. Chem.* **1995**, *396*, 161.